Effects of Location on the Microstructure and Mechanical Properties of Cu-8Al-2Ni-2Fe-2Mn Alloy Produced Through Wire Arc Additive Manufacturing

Wei Chen, Yuhua Chen, Timing Zhang, Taotao Wen, Xiaosong Feng, and Limeng Yin

Wire arc additive manufacturing (WAAM) is successfully applied to the manufacturing of Cu-8Al-2Ni-2Fe-2Mn nickel aluminum bronze alloy. The effects of deposited height on microstructure, tensile properties and microhardness are investigated. Results show that the differences in mechanical properties are related to microstructure anisotropy. The microstructure of the as-deposited condition mainly consists of dendrite, cellular grains, columnar dendrites and equiaxed dendrites. With the increase in height of the deposited wall, the width of the primary dendrite arm spacing successively increases. The microhardness and tensile testing results are differently influenced by the microstructure with the change in positions. The tensile properties, including the ultimate tensile strength and elongation, exhibit anisotropy in the horizontal and vertical directions. The results are explained in detail through temperature field measurement and digital image correlation system. The findings indicate that WAAM is a feasible method to obtain nickel aluminum bronze alloys despite of that fact of anisotropic mechanical characteristics.

1. Introduction

Nickel aluminum bronze (NAB) alloys have been widely used as pipes, valves and pumps casing in marine, chemical and transportation environments because of their high strength, oxidation, corrosion resistance, wear and impact resistance (Ref 1, 2). These multicomponent alloys contain copper (Cu) as the main element, with the addition of aluminum (Al), nickel (Ni), iron (Fe) and manganese (Mn). As the major alloying element, Al content will result in high strength, thereby improving the corrosion resistance and working properties (Ref 2). Ni can improve the corrosion resistance, strength and stability of the microstructure. Fe refines grains and increases the alloy tensile strength, and Mn eliminates brittle temperature range and reduces melting point to improve weldability (Ref 2, 3). Typical casting NAB alloys consist of copper-rich α-Cu phase, four types of intermetallic κ phases (iron-rich $κ_I$, $κ_{II}$, $κ_{IV}$ and nickel-rich $κ_{III}$ phases) and martensitic β phase (Ref 4). The microstructure evolution under equilibrium state can be approximately described as the following distinct stages (Ref 2, 4). The α-Cu phase starts from the β phase around the temperature of 1030 °C. Around the temperature of 930 °C, large precipitates ($κ_I$) are created in the β phase when the wt.% of Fe is greater than five, and another intermetallic globular $κ_{II}$ phase forms with a low level of Fe weight. At 800 °C, the remaining β phase is transformed into the intermetallic $κ_{III}$ phase through a eutectoid reaction. In particular, the saturation solubility of Fe ($κ_{IV}$ phase) will precipitate in the α-Cu matrix when the temperature falls at 860 °C. The martensitic β phase may appear in the NAB alloys under quenching from 1020 °C (Ref 5). NAB alloys are traditionally produced through casting, where porosity and coarse microstructure are inevitable problems that reduce their physical properties and service performance in seawater (Ref 3). Many methods, such as heat treatment (Ref 6), friction stir welding (Ref 7, 8) or friction stir processing (Ref 9) and shot peening (Ref 10), are used to improve the microstructure and mechanical properties of NAB alloys. However, these methods certainly result in increased costs and long manufacturing cycle.

In recent years, wire arc additive manufacturing (WAAM) has gained considerable interests because of its high deposition rate, full density, efficiency and low equipment cost (Ref 11, 12). In WAAM, an electric arc is used as a heat source and utilizes either gas metal arc welding (GMAW) (Ref 13, 14), gas tungsten arc welding (GTAW) (Ref 15, 16) or plasma arc welding (Ref 17) to melt the wire as the feed stock. Compared with casting (casting: 10 K/s) (Ref 4), the cooling rates in WAAM are substantially higher (WAAM: 10^2 K/s) (Ref 18) to obtain fine microstructures. To date, some studies have demonstrated that NAB alloys can be fabricated through WAAM. Ding et al. (Ref 19) first reported the manufacturing of NiAl bronze components using GMAW. They found that the as-deposited metal predominantly contains Widmanstätten α and fine martensite. Additional post-weld heat treatment can refine the microstructure and improve its tensile strength and hardness. Dong et al. (Ref 20) used a twin wire GTAW system to fabricate Cu-Al alloy. Intermetallic phases, such as $CuAl_2$ and Cu_9Al_4, are detected in the as-deposited condition, and the

Wei Chen, Yuhua Chen, Timing Zhang, and **Taotao Wen**, Jiangxi Key Laboratory of Forming and Joining Technology for Aerospace Components, Nanchang Hangkong University, Nanchang 330063, China; **Xiaosong Feng**, Shanghai Aerospace Equipments Manufacturer, Shanghai 200245, China; and **Limeng Yin**, School of Metallurgy and Materials Engineering, Chongqing University of Science and Technology, Chongqing 401331, China. Contact e-mails: 974243230@qq.com and ch.yu.hu@163.com.

contents of intermetallics decrease after homogenization annealing. Shen et al. (Ref 21, 22) obtained the mechanical properties in longitudinal, transverse and normal directions of the deposited Cu-9Al-4.5Ni-3.5Fe-1.3Mn alloy. The results showed that the deposit exhibits higher strength in the longitudinal and transverse directions than in the normal direction. The isotropic microstructure and favorable mechanical properties can be modified through quenching at 900 °C for 2 h and tempering at 675 °C for 6 h. Dharmendra et al. (Ref 23) analyzed that Cu-9Al-4Fe-4Ni-1Mn alloy forms κ_{II} and κ_{III} phases in the interdendritic regions and precipitates κ_{IV} particles within the α-Cu matrix. They also reported that the WAAM samples in as-fabricated condition exhibit considerably higher yield strength (YS) and percent elongation (El) compared with the as-cast samples. The ultimate tensile strength (UTS) is equal to the as-cast alloys. WAAM is suitable to produce NAB alloys. However, no study is reported on the effect of location on the microstructure and mechanical properties of NAB alloys produced through WAAM.

In the present work, WAAM was used to fabricate NAB alloy wall components for studying the effects of location on the microstructure and mechanical properties. Microstructural evolution was investigated in different deposited layers through optical and scanning electron microscopy. The microhardness at different locations was measured with a digital hardness tester. Tensile properties, including the UTS, 0.2% offset YS and El, were evaluated using a universal tensile tester, and the fractured surfaces of the tensile samples were observed through scanning electron microscopy. The microstructure variation and mechanical properties in different regions were explained through temperature field measurement and digital image correlation (DIC) system. These results contribute to understanding the effectiveness of WAAM in producing NAB alloy components.

2. Materials and Methods

The WAAM equipment mainly consists of a welding system (Fronius Transpuls Synergic 2700 welding machines, Fronius, Pettenbach, Austria), a three-dimensional numerical control working table and inert protective gas. The deposition material used in this study was NAB alloy wire with 1.0 mm diameter. The chemical composition of the wire is listed in Table 1, which is usually expressed as Cu-8Al-2Ni-2Fe-2Mn. The substrate was a low-carbon steel plate with dimensions of 150 mm length, 100 mm width and 6 mm height. The substrate surface was cleaned to remove grease and oil with acetone before deposition. Some wall samples were deposited under the parameters of arc current (97 A), arc voltage (10.3 V), welding speed (0.48 m/min), wire feed speed (4.0 m/min), nominal increment of Z axis (2.0 mm), nominal increment of Y axis (3.0 mm) and argon flow rate (15 L/min). The deposition torch tip to work distance was kept to 15 mm, and the contact angle

was 90° for all the experiments. The interlayer dwelling time between each layer was kept at 30 s to enhance the deposited layer. Thermal cycle was measured with a K type thermocouple, and the measuring range of temperatures was between 0 and 1350 °C. Typical fabricated wall samples are presented in Fig. 1(a) and (b). The welding path was alternated back and forth (Fig. 1c and d). The single-bead walls were used to study the effects of location on the microstructure and mechanical properties.

The required specimens were machined with a wire electric discharge machine. The specimens used for metallographic observation and hardness test were cut from the center area (as marked in the dotted line in Fig. 2a). A mixed solution of 5 vol.% ferric chloride, 20 vol.% hydrochloric acid and 75 vol.% distilled water was used to reveal the microstructure of the samples after mounting, grinding and polishing. The microstructures of deposited samples were examined with a Zeiss Axio Scope A1 optical microscope (OM) (Carl Zeiss Microscopy GmbH, Gottingen, Germany), Hitachi SU 1510 scanning electron microscope (SEM) (Hitachi, Tokyo, Japan) and FEI Talos f200 × transmission electron microscope (TEM) (FEI, Hillsboro, OR, USA). X-ray diffraction (XRD) (Axs-D8 Advance, Bruker, Karlsruhe, Germany) analysis was conducted using Cu target at diffraction angle (2θ) from 20° to 90° to identify the phases.

The tensile properties of the deposited wall were measured in the horizontal (welding direction) and vertical directions (deposition direction). The two orientations were referred to as H and V, respectively. The locations and sizes of the tensile specimens are shown in Fig. 2(a) and (b). The produced specimens had the following dimensions: 50 mm overall length, a gage section of 25 mm in length by 5 mm in width and 3 mm in thickness. The tensile properties between the H and V directions were compared. Considering the heterogeneous microstructure within the deposited wall (Ref 24), five specimens were machined in different regions along the deposition direction to reveal the effects of location on the tensile properties (Fig. 2a). A reference as-cast NAB alloy sample, which was close to the composition of the welding wire, was used to test the tensile properties and analyze the microstructure. The as-cast alloy specification corresponded to unified numbering system C95220, and the nominal composition (wt.%) of this material was: Cu: 81% minimum, Al: 8.0-10.5%, Ni: 2.5%, Fe: 2.0-4.0%, Mn: 0.5-2.0%. Tensile tests were performed at room temperature with an extension rate of 0.5 mm min^{-1} using an Instron 8872 universal testing machine (Instron Corporation, Norwood, MA, USA). The strain was measured with an electronic extensometer. The strain evolution of the sample was investigated using an optical system incorporated with DIC system (iX Cameras, Shanghai, China). The test samples were prepared with spray-painted black speckles on a white paint layer providing a random speckle pattern for the DIC system to follow. During the tensile test, the deformation was recorded using the DIC system, and the captured images were analyzed with the help of an in-house software. The fracture surfaces were examined through SEM. Microhardness was measured using a QNESS 10A + semiautomatic Vicker tester with a test load of 50 g and a dwell time of 10 s. Indentations were performed along the vertical centerline (Z) in the cross section (X–Z plane) with an interval of 1.0 mm. Microhardness was measured along the weld direction (Y) in the longitudinal section (Y–Z plane) of the deposited metal (Fig. 2c). Netzsch Sta 449F3 (Netzsch, Selb,
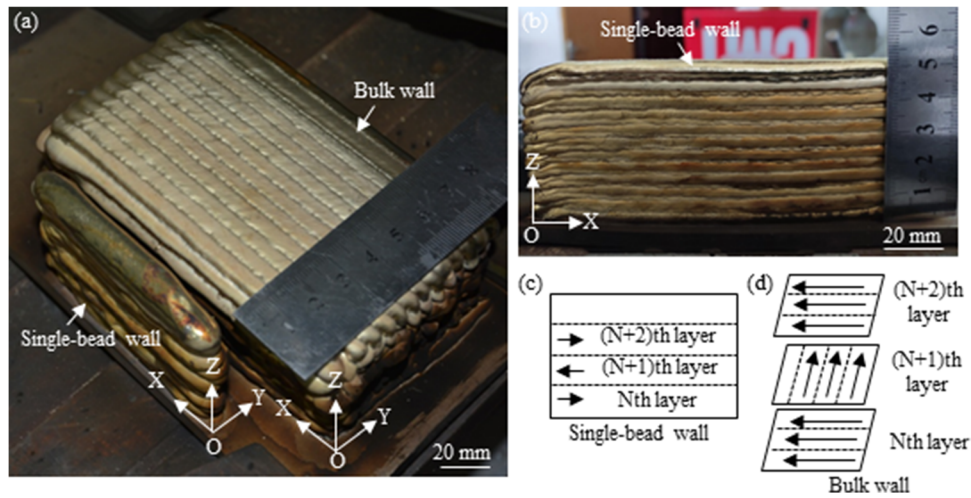
Table 1   Chemical composition of NAB alloy wire (wt.%)

Cu	Al	Ni	Fe	Mn
86	8	2	2	2

Fig. 1 (a) and (b) Typical WAAM fabricated samples, (c) and (d) schematic of the welding path
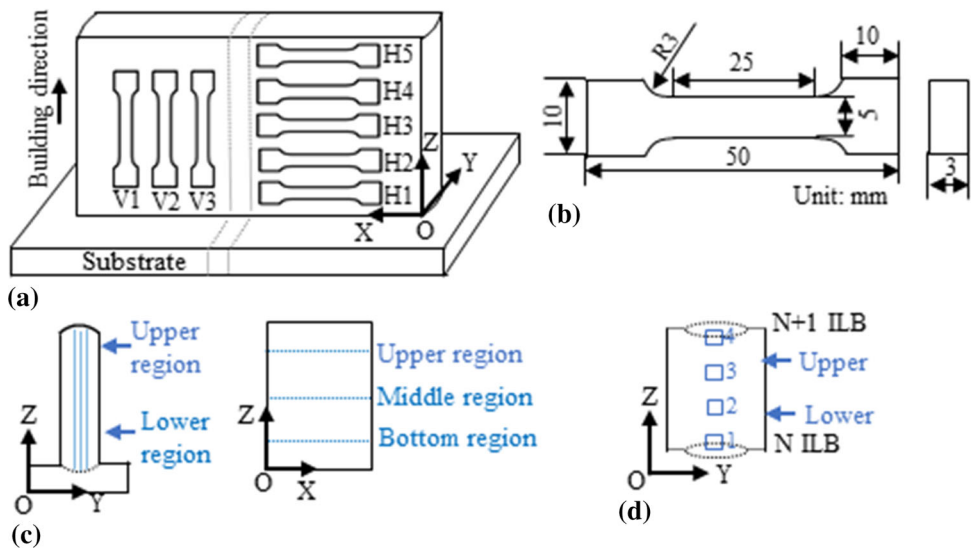

Fig. 2 Schematic configurations of sample preparation: (a) position of tensile specimens, (b) dimensions of tensile specimens in mm, (c) schematic of microstructure observations and microhardness test (blue points marked as hardness indentation) and (d) schematic of microstructure observation position

Germany) differential scanning calorimetry (DSC) was used to study the melting points of WAAM fabricated samples with a heating rate of 10 °C/min.

3. Results

3.1 Microstructure Characteristics and Phase Constituents

The typical macrostructure of the cross section (Y–Z plane) is shown in Fig. 3(a). Typical epitaxial growth of columnar grains is oriented along the deposition direction, which is opposite to the direction of heat flow. The growth direction of the columnar grains is not strictly vertical to the substrate throughout the sample. The cooling of the weld pool primarily occurs via the substrate or previously deposited layer (Ref 25). Hence, the growth direction of the columnar grains appears to be an angle with the substrate. Regularly distributed interlayer bands (ILBs) are uniformly spaced in the entire sample (as

shown in the insert pictures in Fig. 3a). The formation of ILBs can be attributed to the partial remelting of the previously deposited layers by WAAM. The two adjacent ILBs are separated by approximately 2.0 mm, which correspond to the average added layer height. The deposition height of the last layer is more than 2.2 mm, making it convenient to explain that the ILBs are remelted structure. Similar ILB structure has been reported in laser melting deposition (Ref 26) and WAAM (Ref 27).

Figure 3(b) shows the microstructure of the bottom region in the first-pass deposited layer (Y–Z plane). A region of planar growth is found because of the high temperature gradient (G) and slow growth rate (R) at the bonding interface and is indicated by a black arrow (Fig. 3b). WAAM involves a larger melt pool diameter and layer height than power bed technologies, thereby leading to a greater microstructural heterogeneity (Ref 27). Kurz and Fisher indicated that the ratio of G/R determines the growth morphology and G • R controls the scale of formed microstructure (Ref 28). With the decrease in

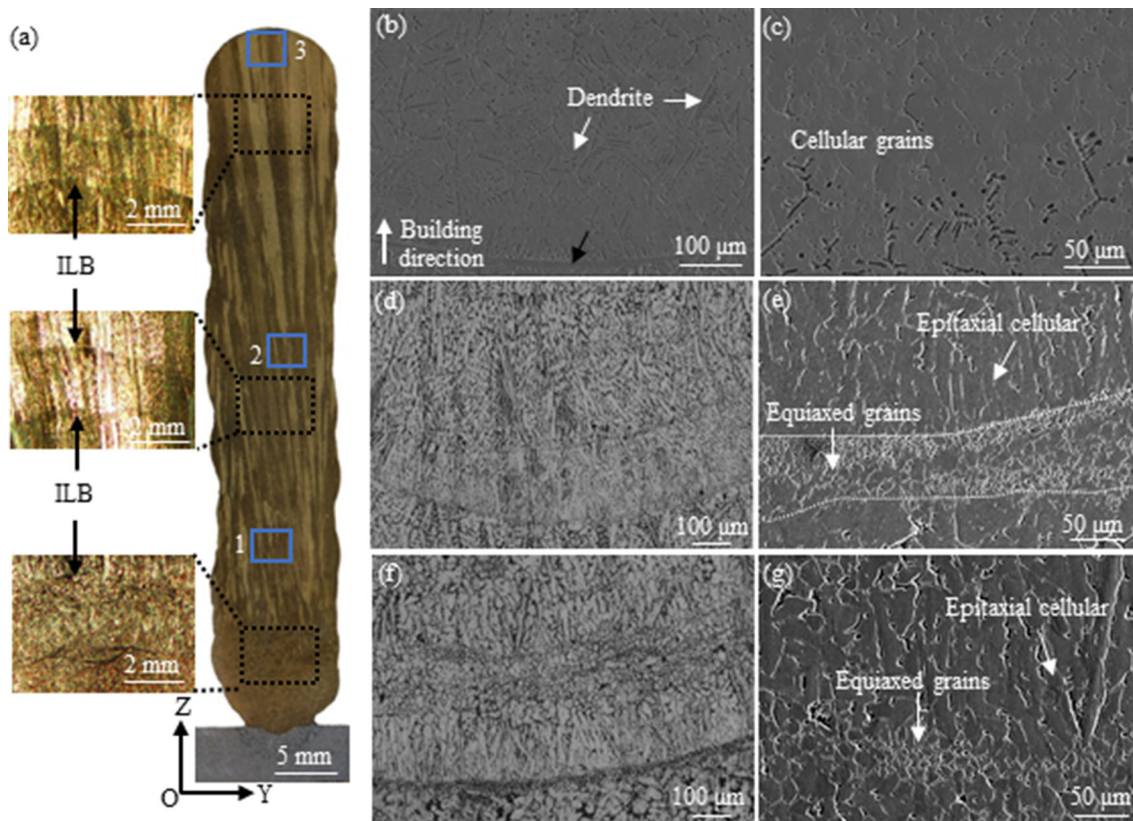**Fig. 3** Morphology and microstructure in the *Y–Z* plane of deposited metal: (a) macrostructure morphology and ILB structure, (b) microstructure in the bottom of first-pass layer, (c) dendritic transforms to cellular grains in the first-pass layer, (d) microstructure in the first ILB zone (OM), (e) enlarged version of Fig. 3(d) (SEM), (f) microstructure in the second ILB zone (OM) and (g) an enlarged version of Fig. 3(f) (SEM)

G/R from the bottom to the top of the molten pool, a dendrite structure forms in the bottom of the molten pool (Fig. 3b) and changes to cellular grains without secondary dendrite arms (SDAs) in the middle of the first-pass deposited layer (Fig. 3c).

In the second-pass deposited layers, epitaxial cellular grains without SDA growth oriented upward grow in the opposite direction to the temperature gradient (Fig. 3d). Some equiaxed grains are stuck in the ILB zone (Fig. 3e). A similar phenomenon occurs in third-pass deposited layer (Fig. 3f and g). This condition is probably because the thermal environment is dynamic during additive manufacturing and equiaxed grains are only formed when temperature gradients sufficiently decrease to permit constitutional supercooling (Ref 29). After the deposition of third-pass layers, the epitaxial columnar grains form in the subsequent regions.

The changes in columnar grains are usually related to the deposition height. Figure 4 shows the OM micrographs of the microstructure between two adjacent ILBs in different deposited heights (the *Y–Z* plane presents the grain morphology in the bottom, middle and top regions of the columnar grains, and the observation position is shown in the blue box in Fig. 2d and 3a). The microstructure of the Cu-8Al-2Ni-2Fe-2Mn alloy is mainly composed of abundant fine columnar dendrites caused by high cooling during solidification in WAAM and grows epitaxially along the deposition direction with some equiaxed grains located at the sides of columnar dendrites, as shown in Fig. 4(a1–a4, b1–b4 and c1–c3). The width of the primary dendrite arm (PDA) spacing from the bottom to the top region successively increases. The PDA spacings of the

measured near-substrate, middle and top regions are 14.5 ± 4.5, 23.6 ± 5.2 and 29.8 ± 5.5 μm, respectively. With the dynamics of *G/R* in the weld pool, regular small SDA formation can be observed in each deposited layer. The secondary dendrites are nearly perpendicular to the primary dendrites and serve as growth sites for the primary dendrites of the next layer as they follow the heat flux direction. This condition probably helps to maintain the growth direction of primary dendrites in subsequent layers (Ref 30). In the last-pass deposited layer, the grain morphology changes from columnar dendrites to equiaxed dendrites because of the decrease in temperature gradient and the increase in interface moving velocity (Ref 31). No subsequent layers remelt the grains, and only the top region shows this transition characteristic (Fig. 4c4).

Metallographic examination indicates that similar columnar dendrite change occurs in the *X–Z* plane (Fig. 5). With the decrease in the G/R ratio from the bottom to the top of the welding pool, the microstructure transforms to columnar dendrites with secondary arms. The width of PDA spacing increases with the deposited height.

The typical microstructure of the *X–Y* plane is shown in Fig. 6. The microstructure appears as coarse primary columnar grains at low magnification because it grows epitaxially along the deposition direction (as shown by the dotted lines in Fig. 6a). In the lower region (the observation location is marked with a blue arrow in Fig. 2c), typical equiaxed grains are found in the bottom of the welding pool, which is upper than the ILB (as shown in Fig. 6b and d, the observation
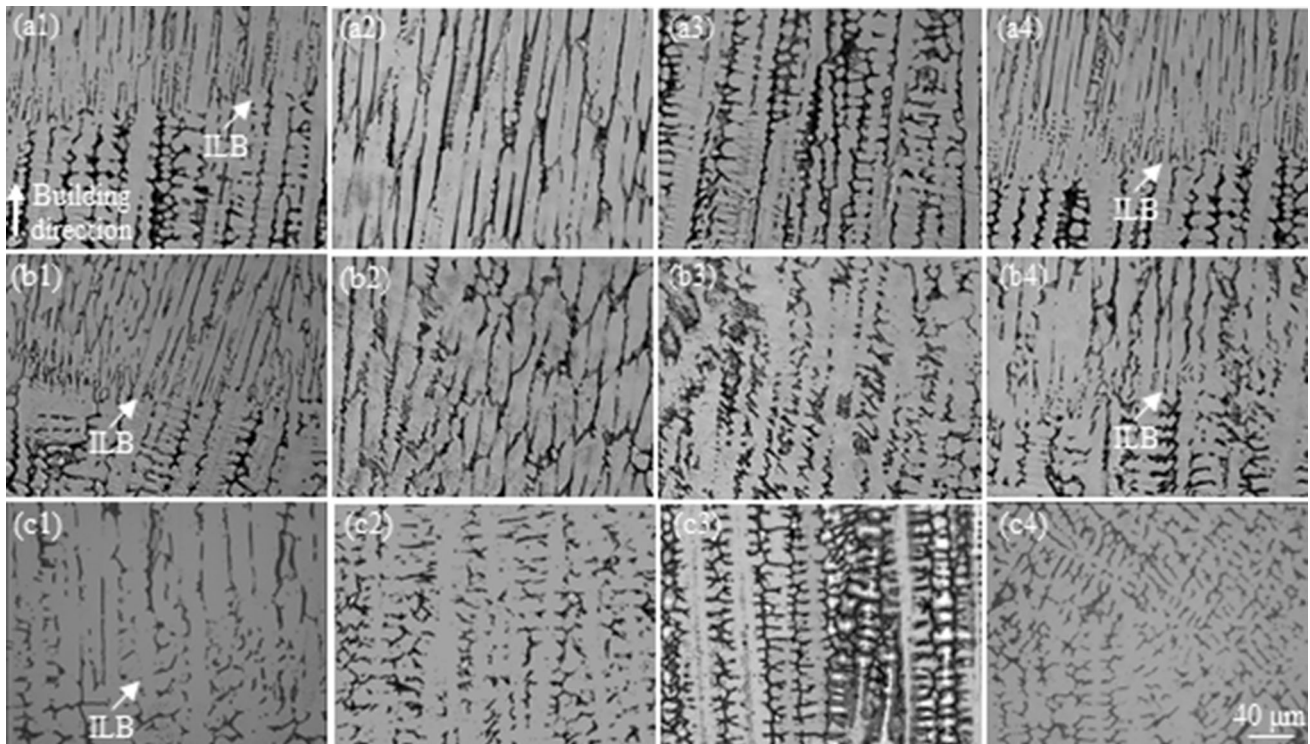
Fig. 4 Effect of deposited height on the microstructure between two adjacent ILBs in the columnar grains (*Y–Z* plane): (a1)–(a4), (b1)–(b4), (c1)–(c4), representative of the microstructure from box 1-box 3 in Fig. 3(a), respectively
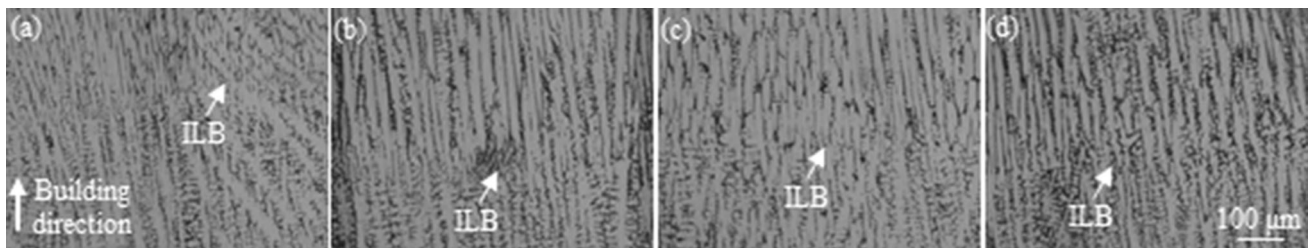

Fig. 5 Effect of deposited height on the microstructure of the ILB region (*X–Z* plane): (a)-(d) represent the microstructure from the bottom to the top region in the columnar grains

location is marked with a blue arrow in Fig. 2d). The microstructure transforms to dendritic structures because of the development of SDA (Fig. 6c and e). With the accumulation of heat, the grain size in the upper region is larger than that in the lower region. The transition microstructure in the *X–Y* plane demonstrates that the transformed dendrites are equiaxial dendrites rather than the columnar dendrites along the welding direction.

The results of XRD phase characterization in different locations of deposited wall are shown in Fig. 7. The deposited wall mainly involves the diffraction peaks of α-Cu phase and small amounts of intermetallic phases (κ phase) caused by alloying elements, such as Al, Ni and Fe. Compared with different deposited heights, the diffraction peak broadens in the lower region, as indicated by red arrows in Fig. 4. This finding can be attributed to fine grain structure in this region, which is reported in a previous literature (Ref 32). The diffraction peak in the bottom region does not accord with the regularity of the columnar grains mainly because of the difference in microstructure.

OM examination did not reveal any intermetallic phases in WAAM samples. Figure 8 shows the TEM image of the WAAM Cu-8Al-2Ni-2Fe-2Mn alloy at high magnifications, revealing some globular κ_{II} based on Fe$_3$Al and lamellar κ_{III} based on NiAl in the interdendritic region (Fig. 8a and b). Some amounts of fine κ_{IV} (rich-Fe, 5 nm to 10 nm in size) precipitates are observed in the α-Cu matrix (Fig. 8c). These small and disperse κ_{IV} phases may inhibit grain boundary mobility, which is beneficial for improving strength (Ref 33). The results are similar to those reported by other studies (Ref 4, 23). No evidence of retained β martensite or κ_{I} phases is observed in the WAAM samples. The microstructural examination of the as-cast C95220 alloy found that a number of intermetallic particles are dispersed in the relatively coarse α-Cu matrix. As shown in the SEM micrograph in Fig. 8(d), the intermetallic phases consist of large κ_{I} in rosette morphology, κ_{II} in the form of small roughly globular particles, κ_{III} in lamellar morphology and κ_{IV} in the form of numerous fine particles homogeneously precipitated within the α-Cu matrix (Ref 4, 34).
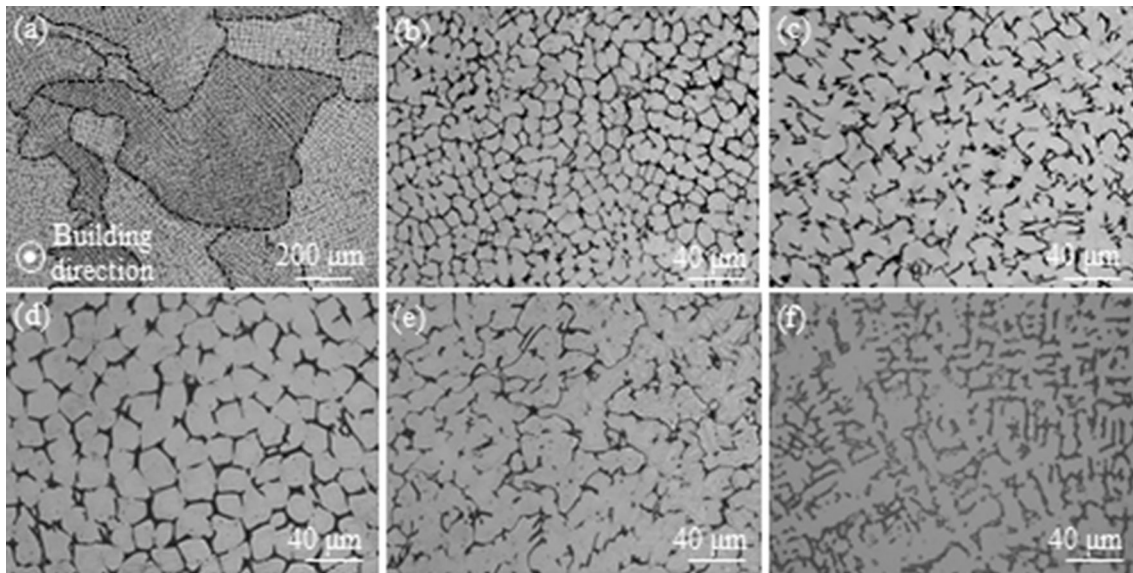
Fig. 6 Effect of deposited height on the microstructure in the *X–Y* plane: (a) low magnification of primary columnar grains, (b), (c) microstructure of different locations in the same deposited layer at the lower region, (d), (e) microstructure of different locations in the same deposited layer at the upper region and (f) microstructure in the transition region (the top of last layer)
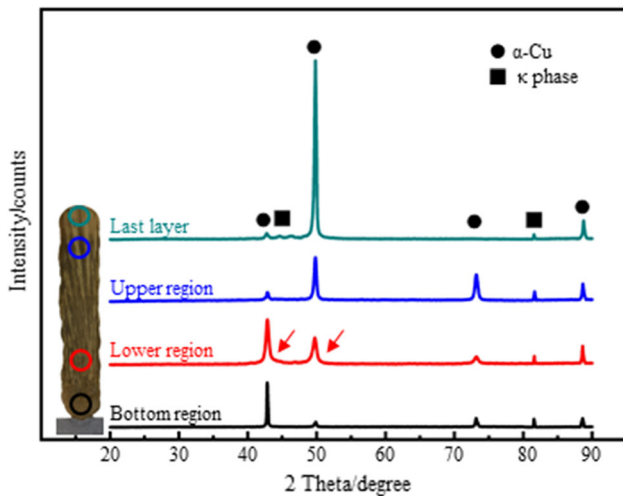

Fig. 7 XRD patterns of WAAM Cu-8Al-2Ni-2Fe-2Mn alloy in different deposited heights

3.2 Tensile Properties and Microhardness

Tensile properties are tested in the horizontal (*H*) and vertical directions (*V*). The stress–strain curves for the *H* and *V* directions in the WAAM samples and as-cast C95220 alloy and the tensile properties determined from these curves are compared in Fig. 9. All of the WAAM samples are found to exhibit considerably higher YS and El compared with the cast samples. Cast C95220 alloy has UTS than that of WAAM samples because of its more contents of Al, Fe and Ni. In the perspective of NAB component engineering design, YS is more relevant than UTS. The stress–strain curves demonstrate that although the nature of the flow curves of samples in the H and V directions is similar, a marked difference is found in their properties. The UTS of the *H* direction (424-458 MPa) is higher than that of the V direction (401-405 MPa). The YS of the V direction (192-193 MPa) is comparable to that of the H

direction (190-195 MPa). Regarding ductility, the El of the *V* direction (43.32-47.11%) exhibits higher ductility than the *H* direction (40.52-41.77%). The anisotropy of UTS and El exists in the WAAM samples. The detailed results of the average tensile properties (including standard deviation) in the vertical and horizontal directions within the UTS, YS and El are listed in Table 2.

The tensile properties at different heights along the deposition direction are tested (the location of tensile specimen is consistent with that of Fig. 2a) to study different locations along the deposition direction on the tensile properties of the deposited wall. The experimental results are shown in Fig. 10. The location near the substrate section of the deposited wall shows the highest UTS, YS and ductility because of the fine cellular grains. The UTS and YS are sensitive to the locations, and the PDA spacing increases with the increase in deposition direction, as shown in Fig. 4, 5 and 6. Thus, the UTS and YS values gradually decrease from the near-substrate to the top region. Ductility exhibits minimal variation in different deposited heights. These tensile test results are consistent with the change in microstructure.

Figure 11 shows the SEM micrographs of the tensile fracture surfaces for the WAAM samples and as-cast C65220 alloy. The WAAM samples in V and H directions and as-cast C95220 alloy have extremely different fractures. For the WAAM alloy sample in V direction, the dimples and slip separation (marked by white arrow in Fig. 11a) are mixed. The WAAM alloys of H1 sample are mainly dominated by dimples in terms of fracture (Fig. 11b). Samples H2 to H5 show extremely similar fracture, the fracture surface morphology exhibits a transgranular ductile failure mode, the dimples are found in the boundaries, and the PDAs are clearly observed (Fig. 11c–e). The PDA spacing in the fracture increases with different heights along the deposition direction, which is consistent with the results of microstructure observation (as shown in Fig. 4, 5 and 6). The fracture morphologies of tensile specimens at different heights are consistent with the tensile properties. The fracture surface of as-cast samples shows some
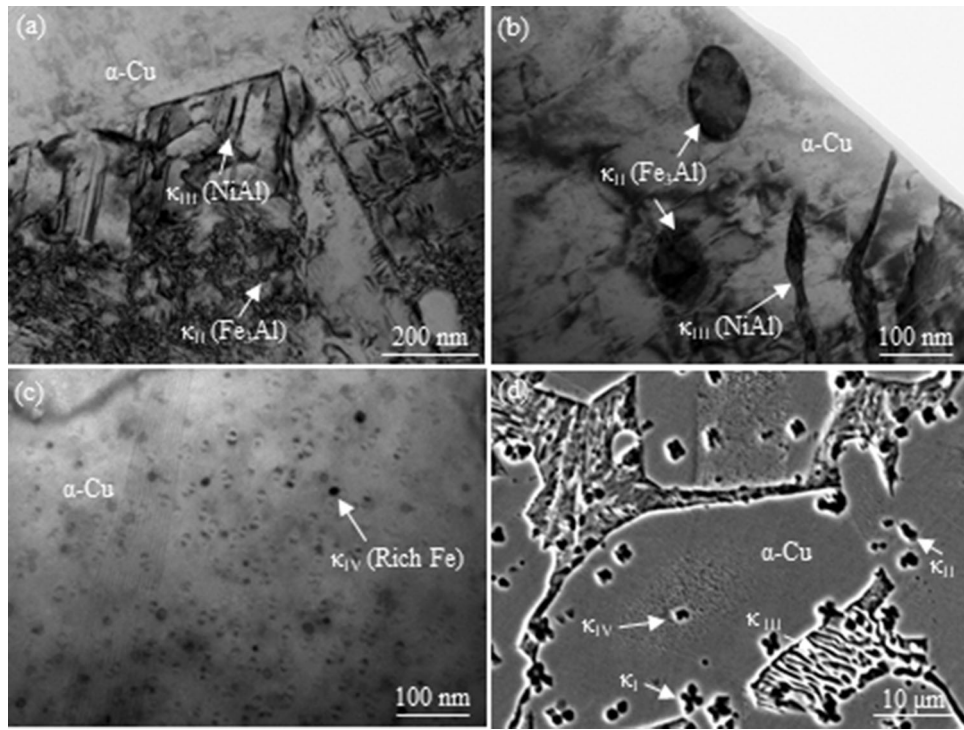
Fig. 8 Intermetallic phases in NAB alloys: (a) and (b) TEM images of WAAM samples in the interdendritic regions, (c) TEM images of WAAM samples in the α-Cu matrix and (d) SEM images of cast C95220 alloy
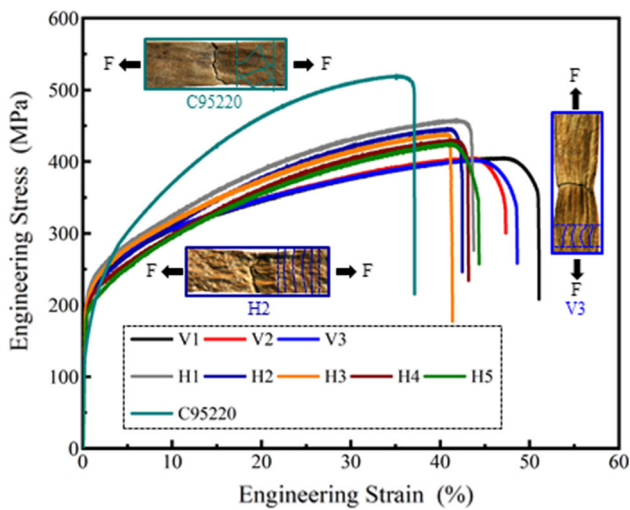

Fig. 9 Comparison of stress–strain curves of as-cast C95220 alloy and WAAM samples (inserted pictures represent the relationship between applying tension and grain direction in the samples, where F denotes tensile force direction)

Table 2 Tensile properties of the WAAM samples

Direction	UTS, MPa	YS, MPa	El, %
Horizontal	439.87 ± 11.81	192.53 ± 1.68	41.05 ± 0.43
Vertical	403.15 ± 1.55	193.08 ± 0.76	44.64 ± 1.74

regions with flat fracture that adverse to the ductility (Fig. 11f), the fracture mode shows a mixture of regions of small dimples with the regions of cleavage facets.
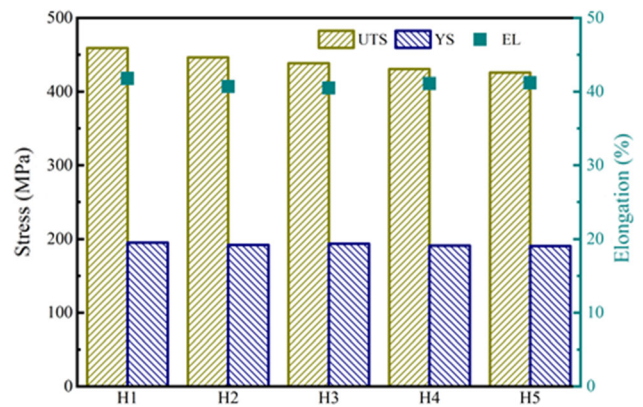

Fig. 10 Effect of location on the tensile properties and El of deposited metal in different regions corresponding to Fig. 2

The changes in microhardness values along the deposited height in the X–Z and Y–Z planes are shown in Fig. 12. Figure 12(a) displays the microhardness values from the bottom region to the top region along the centerline (as shown in the schematic graph in Fig. 2c). The hardness values near the bottom region are higher than the middle and top regions. The maximum microhardness values are found near the bottom area, which can be attributed to the cellular grains near the bottom region. The hardness fluctuation range of the columnar grains and equiaxed dendrites is smaller compared with the bottom region. Figure 12(b) shows the microhardness values of columnar grains at different locations along the deposition direction in the X–Z plane, with the corresponding locations of testing lines marked in Fig. 2c. The mean hardness values of the bottom, middle and top regions are 139.8 ± 1.7 HV, 135.4 ± 1.6 HV and 131.2 ± 1.9 HV, respectively. The
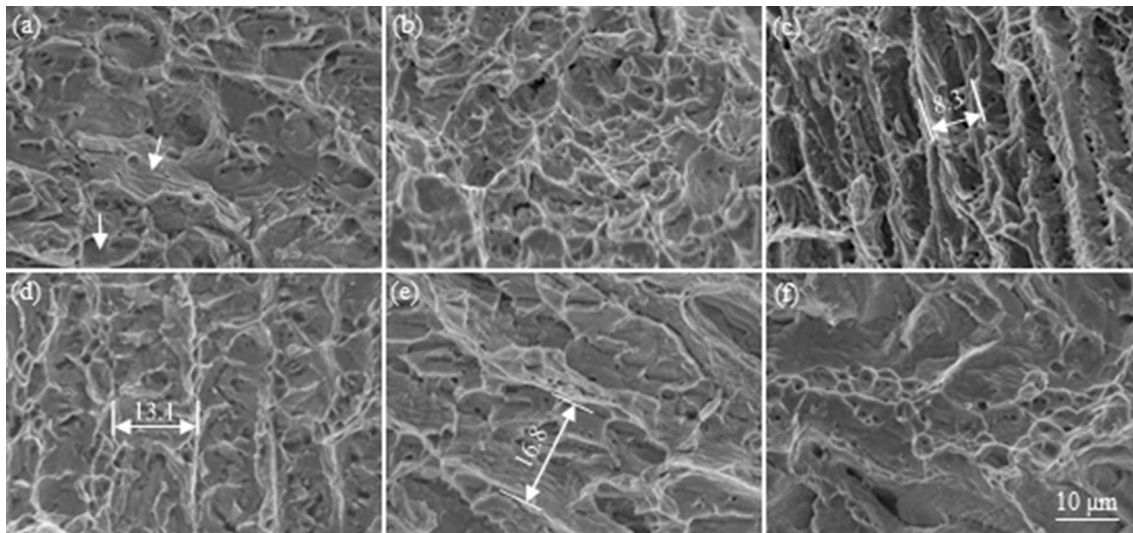
Fig. 11 Fracture surfaces of tensile samples: (a) V3 sample, (b) H1 sample, (c) H2 sample (d) H4 sample (e) H5 sample and (f) as-cast sample (the white arrow indicates the characteristics of slip separation)
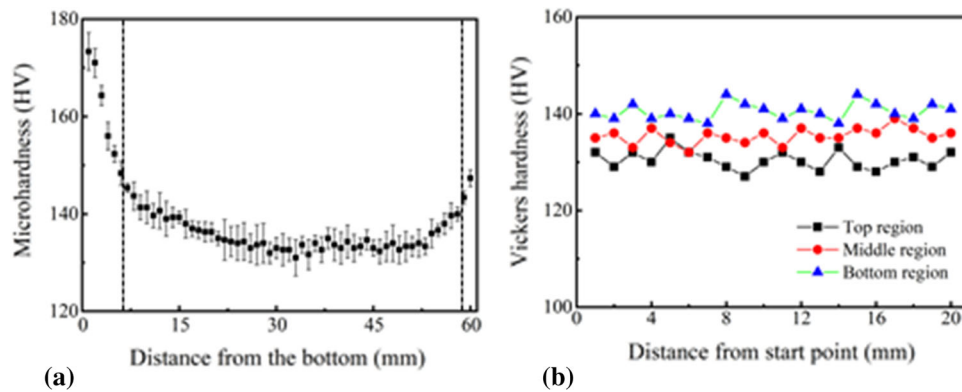

Fig. 12 Microhardness distribution of the deposited WAAM metal: (a) *Y–Z* plane and (b) *X–Z* plane

microhardness tends to be relatively homogeneous along the welding direction at the same height, that is, no difference is observed in the microstructure along the welding direction at the same height. For different deposition heights, the heat accumulation of the deposited metal and the cooling rate are different, thereby directly affecting the PDA spacing and resulting in a large difference in the hardness between different heights. The consistency of these microhardness measurement results is in agreement with the tensile test.

4. Discussion

The microstructure transformation of Cu-8Al-2Ni-2Fe-2Mn alloy in the deposited metal can be mainly affected by solidification conditions. Temperature gradient G and growth rate V dominate the mode of solidification (Ref 28). With the variations in G and V, various microstructures, such as dendrite morphology, cellular grains, columnar dendrites, secondary dendrites and equiaxed dendrites, can be generated.

The typical thermal history measured in WAAM for a sequence of 20 deposited layers is shown in Fig. 13. A type-K thermocouple is buried 2 mm below the surface of the substrate

in a hole. After the deposition of the first- and tenth-pass layers, the thermocouples are quickly plunged into the melt pool and record the subsequent deposited layer thermal cycle. As shown in Fig. 13(a), the substrate temperature reaches its maximum at the fourth-pass layer with the increases in deposited height (the black arrow in Fig. 13a). This finding shows that the substrate has a great influence on the microstructure during the deposition of the first third-pass layers. The cooling rate of first third-pass layers near the substrate is quicker than those of the subsequent layers. The region of dendritic structure forms at the bottom of the molten pool in the first-pass layer because of the high temperature gradient and slow growth rate (Fig. 3b). Cellular grains are found in the upper region of the first-pass layer and the second-pass deposited layer (Fig. 3c and d). Cellular grains, which are usually ellipsoid-like crystals, grow perpendicular to the heat flux direction (Ref 35). The spacing among the cellular structure varies. The initial cellular morphology can adjust itself to give an optimum growth (Ref 36).

Comparing the peak temperature of the first- and tenth-pass layers, the peak temperature slightly increases with the increase in deposited height (Fig. 13a). The arc heat does not have sufficient time to transmit, and more heat accumulation occurs in the upper layer, thereby reducing the temperature gradient and increasing the PDA spacing. The peak temperature of the
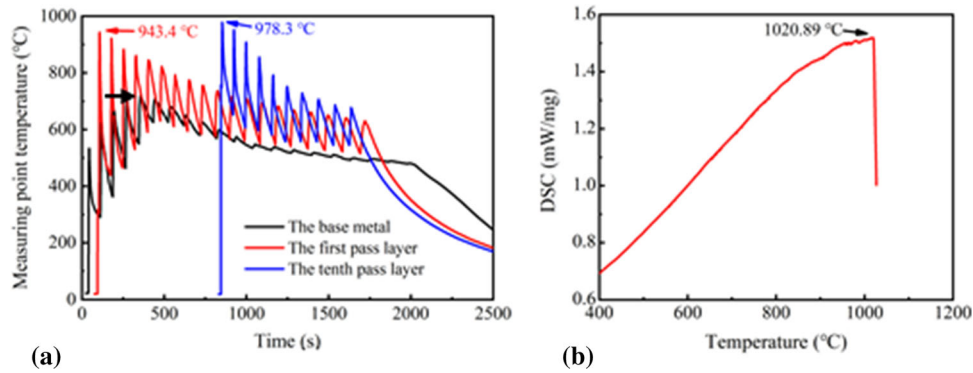
Fig. 13 (a) Temperature field for different regions and (b) DSC curve of the WAAM Cu-8Al-2Ni-2Fe-2Mn alloy

curve is extremely close to the melting point (1020.89 °C) measured through DSC (Fig. 13b). Hence, we can predict that the temperature of the arc melting pool is sufficiently high to remelt the equiaxed dendrites (Fig. 4c4), and the SDAs help to maintain the growth direction of primary dendrites in subsequent layers (Fig. 4a1-b4 and c1-c3) and form the epitaxial growth.

The product of temperature gradient G and growth rate V governs the mode of dendritic arm spacing. According to Kurz and Fisher's model (Ref 28), PDA spacing λ can be expressed as:

$$\lambda = \left(\frac{3\Delta T_0 R}{G}\right)^{\frac{1}{2}} \quad (Eq\ 1)$$

where ΔT_0 is the non-equilibrium solidification range and R is the dendrite tip radius. Dendrite tip radius R can be expressed as:

$$R = \pi \left(\frac{4D_L \Gamma}{K\Delta T_0 V}\right)^{\frac{1}{2}} \quad (Eq\ 2)$$

where D_L is the liquid diffusion coefficient, Γ is the Gibbs–Thomson coefficient and K is the equilibrium diffusion coefficient. PDA spacing λ is identified as a function of G and V and can be expressed as:

$$\lambda = \left(\frac{3\pi}{G}\right)^{\frac{1}{2}}\left(\frac{4D_L T_0 \Gamma}{KV}\right)^{\frac{1}{4}} \quad (Eq\ 3)$$

In accordance with Eq 3, the lower the value of $G \times V$ is, the greater the possibility of large dendritic arm spacing formation will be. As previously described about temperature field, the temperature gradient and cooling rate decrease, accompanied by an increase in the PDA spacing, when the deposited height increases. On the basis of this discussion and the Hall–Petch relationship (Ref 37), large dendritic arm spacing in the top region provides an explicit explanation for the lower tensile strength and microhardness than that in the middle and near-substrate regions.

The strain maps obtained under the tensile loading in the horizontal and vertical directions are presented in Fig. 14. A consistent scale ranging from quarter, half, three quarters and final fracture is used to facilitate the comparison. Different colors in the gauge section indicate different deformation degrees. As indicated in the vertical sample, the deformation of

inhomogeneous microstructure in the columnar grains starts with the elastic deformation stage (Fig. 14a1). With the increase in tensile load, inhomogeneous deformation among ILBs can be observed (Fig. 14a2). The strain concentrations occur in the weak region of the sample. The large plastic strain (red region) of 930 s indicates two possible regions where necking may occur (Fig. 14a3). Fracture occurs in the necking location (Fig. 14a4). The horizontal sample exhibits uniform deformation during tension (Figs. 14b1 and b2). In the plastic deformation stage, the fracture will eventually occur when a large deformation is formed (Fig. 14b3 and b4). A previous study showed that the strength is related to the growth of columnar grains along the deposition direction (Ref 38). The discrepancies in El and strength between H and V directions can be attributed to the coarse columnar grains. The vertical specimen contains many columnar grains, and the horizontal specimen contains many columnar grain boundaries (as shown in the insert test samples pictures in Fig. 9). Considering that the strength caused by the grain boundaries is higher than the strength from the grains themselves (Ref 39), the tensile load perpendicular to the grain boundaries leads to a greater load to separate the adjacent columnar grains (Ref 40). Thus, the strength of the horizontal tensile specimen is higher than the vertical one.

As shown in the inserted test samples pictures in Fig. 9, the vertical samples show more obvious uniform El and necking compared with the horizontal samples, indicating that vertical samples have greater plastic deformation and lead to slip separation and dimple on the fracture (Fig. 11a). The fractures change to transgranular with dimples with the increase in strength and decrease in El (Fig. 11b–e). The existence of columnar grains and the width of the primary dendrite that changes with position in the deposited metal are the primary factors of anisotropy in tensile properties.

WAAM is successfully applied to NAB components with complicated structure and shape. Compared with casting and additive manufacturing methods, the mechanical properties of as-deposited Cu-8Al-2Ni-2Fe-2Mn alloy display a combination of UTS and ductility (Ref 19–23, 41, 42) (Fig. 15). WAAM is relatively low-cost technology, and NAB alloys can be additively manufactured with designed different components of welding wire to obtain the corresponding properties. Although the proposed methodology is applicable to NAB alloys, many studies should be conducted, especially for corrosion behavior, wear, impact properties, fatigue properties
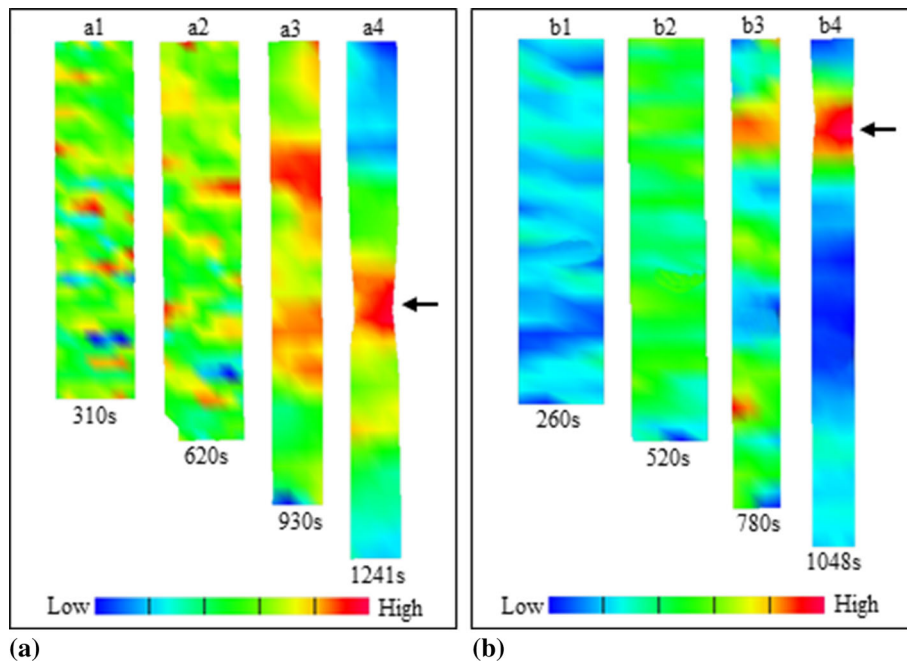
Fig. 14 Strain maps obtained from the DIC measurements: (a) vertical direction sample and (b) horizontal direction sample (The black arrow denotes fracture position. For interpretation of the references to color in this figure, the reader can refer to the web version of this article.)
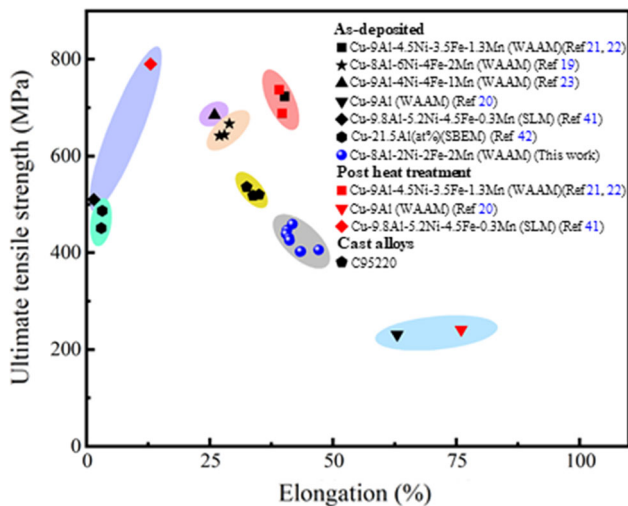

Fig. 15 UTS versus tensile El to failure for NAB alloys fabricated via additive manufacturing and casting

and an excellent combination of improved ductility and high tensile strength in the near future.

5. Conclusions

In this study, full-density Cu-8Al-2Ni-2Mn-2Fe alloy is successfully produced through WAAM. The effects of location on the microstructure and mechanical properties of the wall component are systematically investigated. The major conclusions the present study can be summarized as follows:

(1) The as-deposited walls can be divided into four distinct regions along the vertical deposition direction. In the near-substrate region, the microstructure mostly consists of dendrite and cellular grains. In the third interlayer bands and subsequent deposited layers, columnar dendrites grow epitaxially along the deposition direction, and the equiaxed dendrites form at the top of the deposited layer.

(2) WAAM alters the microstructure, the alloy has an interdendritic microstructure containing globular κ_{II} phase based on Fe_3Al and lamellar κ_{III} phase based on NiAl, and the κ_{IV} phase (rich-Fe) of precipitates is nucleated in the α-Cu matrix. No κ_I and retained β phases are observed in the WAAM alloy.

(3) The PDA spacings of the near-substrate, middle and the top regions are 14.5 ± 4.5, 23.6 ± 5.2 and 29.8 ± 5.5 μm, which are consistent with the decrease in tensile properties and increase in deposited height. The tensile properties differ by approximately 8.3% in the horizontal and vertical directions because of the anisotropic microstructure in these orientations. Compared with the vertical direction, the tensile strength tested in the horizontal direction exhibits higher value but reduced ductility.

(4) The microhardness of the deposited alloy gradually decreases from approximately 175-130 HV with the increase in distance away from the top surface. The microhardness fluctuation range of the middle and top regions is smaller compared with the bottom region.

(5) The fracture surfaces mainly exhibit typical ductile mode fracture characterized with transgranular, dimples and slip separation.

References

1. W.S. Li, Z.P. Wang, Y. Lu, and L.H. Yuan, Corrosion Wear Behavior of Al-Bronzes in 3.5% NaCl Solution, *J. Mater. Eng. Perform.*, 2006, **15**(1), p 102–110
2. S. Fonlupt, B. Bayle, D. Delafosse, and J. Heuzeb, Role of Second Phases in the Stress Corrosion Cracking of a Nickel-Aluminium Bronze in Saline Water, *Corros. Sci.*, 2005, **47**(11), p 2792–2806
3. J.A. Wharton, R.C. Barik, G. Kear, R.J.K. Wood, K.R. Stokes, and F.C. Walsh, The Corrosion of Nickel-Aluminium Bronze in Seawater, *Corros. Sci.*, 2005, **47**(12), p 3336–3367
4. F. Hasan, A. Jahanafrooz, G.W. Lorimer, and N. Ridley, The Morphology, Crystallography, and Chemistry of Phases in as-cast Nickel-Aluminum Bronze, *Metall. Mater. Trans. A*, 1982, **13**(8), p 1337–1345
5. F. Hasan, G. Lorimer, and N. Ridley, Crystallography of Martensite in a Cu-10Al-5Ni-5Fe Alloy, *J. Phys.*, 1982, **43**, p 653–658
6. Z. Wu, Y.F. Cheng, L. Liu, W. Lv, and W. Hu, Effect of Heat Treatment on Microstructure Evolution and Erosion-Corrosion Behavior of a Nickel-Aluminum Bronze Alloy in Chloride Solution, *Corros. Sci.*, 2015, **98**, p 260–270
7. T. Küçükömeroğlu, E. Şentürk, L. Kara, G. İpekoğlu, and G. Çam, Microstructural and Mechanical Properties of Friction Stir Welded Nickel-Aluminum Bronze (NAB) Alloy, *J. Mater. Eng. Perform.*, 2016, **25**(1), p 320–326
8. S. Siva, S. Sampathkumar, and J. Sudha, Microstructure and Mechanical Properties of Exothermic Reaction-Assisted Friction-Stir-Welded Nickel-Aluminum Bronze Alloy, *J. Mater. Eng. Perform.*, 2019, **28**(4), p 2256–2270
9. M.D. Fuller, S. Swaminathan, A.P. Zhilyaev, and T.R. McNelley, Microstructural Transformations and Mechanical Properties of Cast NiAl Bronze: Effects of Fusion Welding and Friction Stir Processing, *Mater. Sci. Eng. A*, 2007, **463**, p 128–137
10. B.J. Zhao, Y.T. Lv, Y. Ding, L.Q. Wang, and W.J. Lu, The Grain Refinement Mechanisms of Various Phases in Shot-peened Nickel-Aluminum Bronze (NAB) Alloy, *Mater. Charact.*, 2018, **144**, p 77–85
11. W.E. Frazier, Metal Additive Manufacturing: A Review, *J. Mater. Eng. Perform.*, 2014, **23**(6), p 1917–1928
12. Y. Zhang, L.M. Wu, X.Y. Guo, S. Kane, Y.F. Deng, Y.G. Jung, J.H. Lee, and J. Zhang, Additive Manufacturing of Metallic Materials: A Review, *J. Mater. Eng. Perform.*, 2018, **27**(1), p 1–13
13. X. Xu, J. Ding, S. Ganguly, C. Diao, and S. Williams, Preliminary Investigation of Building Strategies of Maraging Steel Bulk Material Using Wire + Arc Additive Manufacture, *J. Mater. Eng. Perform.*, 2019, **28**, p 594–600
14. X. Xing, G. Qin, Y. Zhou, H. Yu, L. Liu, L. Zhang, and Q. Yang, Microstructure Optimization and Cracking Control of Additive Manufactured Bainite Steel by Gas Metal Arc Welding Technology, *J. Mater. Eng. Perform.*, 2019, **28**, p 5138–5145
15. J.Y. Bai, C.L. Fan, S.B. Lin, C.L. Yang, and B.L. Dong, Mechanical Properties and Fracture Behaviors of GTA-Additive Manufactured 2219-Al After an Especial Heat Treatment, *J. Mater. Eng. Perform.*, 2017, **26**, p 1808–1816
16. H. Geng, J. Li, J. Xiong, X. Lin, and F. Zhang, Geometric Limitation and Tensile Properties of Wire and Arc Additive Manufacturing 5A06 Aluminum Alloy Parts, *J. Mater. Eng. Perform.*, 2017, **26**, p 621–629
17. B. Lu, X. Cui, M. Dong, W. Ma, and G. Jin, The Influence of Solution Treatments on the Microstructure, Phase Transformation Behavior, and Superelastic Characteristics of Nitinol Synthesized by Plasma Arc Deposition, *J. Mater. Eng. Perform.*, 2020, **29**, p 2491–2498
18. V.D. Facginotti, A. Cardona, B. Baufeld, and O.V. Biest, Finite-Element Modelling of Heat Transfer in Shaped Metal Deposition and Experimental Validation, *Acta Mater.*, 2012, **60**(19), p 6621–6630
19. D.H. Ding, Z.X. Pan, S.V. Duin, H.J. Li, and C. Shen, Fabricating Superior NiAl Bronze Components through Wire Arc Additive Manufacturing, *Materials*, 2016, **9**(8), p 652
20. B.S. Dong, Z.X. Pan, C. Chen, Y. Ma, and H.J. Li, Fabrication of Copper-Rich Cu-Al Alloy Using the Wire-Arc Additive Manufacturing Process, *Metall. Mater. Trans. B*, 2017, **48**, p 3143–3151
21. C. Shen, Z. Pan, D. Ding, L. Yuan, N. Nie, Y. Wang, D. Luo, D. Cuiuri, S. Duin, and H. Li, The Influence of Post-Production Heat Treatment on the Multi-Directional Properties of Nickel-Aluminum Bronze Alloy Fabricated using Wire-Arc Additive Manufacturing Process, *Addit. Manuf.*, 2018, **23**, p 411–421
22. C. Shen, G. Mu, X. Hua, F. Li, D. Luo, X. Li, and C. Zhang, Influences of Postproduction Heat Treatments on the Material Anisotropy of Nickel-Aluminum Bronze Fabricated Using Wire-Arc Additive Manufacturing Process, *Int. J. Adv. Manuf. Technol.*, 2019, **103**, p 3199–3209
23. C. Dharmendra, A. Hadadzadeh, B.S. Amirkhiz, G.D. Janaki Ram, and M. Mohammadi, Microstructural Evolution and Mechanical Behavior of Nickel Aluminum Bronze Cu-9Al-4Fe-4Ni-1Mn Fabricated through Wire-Arc Additive Manufacturing, *Addit. Manuf.*, 2019, **30**, p 100872
24. J.F. Wang, Q.J. Sun, H. Wang, J.P. Liu, and J.C. Feng, Effect of Location on Microstructure and Mechanical Properties of Additive Layer Manufactured Inconel 625 using Gas Tungsten Arc Welding, *Mater. Sci. Eng., A*, 2016, **676**, p 395–405
25. E. Brandl, V. Michailov, B. Viehweger, and C. Leyens, Deposition of Ti-6Al-4 V Using Laser and Wire, Part I: Microstructural Properties of Single Beads, *Surf. Coat. Technol.*, 2011, **206**(6), p 1120–1129
26. Y. Zhu, X. Tian, J. Li, and H. Wang, Microstructure Evolution and Layer Bands of Laser Melting Deposition Ti-6.5Al-3.5Mo-1.5Zr-0.3Si Titanium Alloy, *J. Alloys Compd.*, 2014, **616**(15), p 468–474
27. A. Ho, H. Zhao, J.W. Fellowes, F. Martina, A.E. Davis, and P.B. Prangnella, On the Origin of Microstructural Banding in Ti-6Al4 V Wire-Arc Based High Deposition Rate Additive Manufacturing, *Acta Mater.*, 2019, **166**, p 306–323
28. W. Kurz and D.J. Fisher, *Fundamentals of Solidification*, Trans. Tech. Publications, Zurich, Switzerland, 1986
29. M.J. Bermingham, D.H. StJohn, J. Krynen, S. Tedman-Jones, and M.S. Dargusch, Promoting the Columnar to Equiaxed Transition and Grain Refinement of Titanium Alloys During Additive Manufacturing, *Acta Mater.*, 2019, **168**, p 261–274
30. M. Kaplan and A.K. Yildiz, The Effects of Production Methods on the Microstructures and Mechanical Properties of an Aluminum Bronze, *Mater. Lett.*, 2003, **57**(28), p 4402–4411
31. Q. Li, X. Lin, F. Liu, F. Liu, and W. Huang, Microstructural Characteristics and Mechanical Properties of Laser Solid Formed K465 Superalloy, *Mater. Sci. Eng. A*, 2017, **700**, p 649–655
32. Y. Lv, L. Wang, Y. Han, X. Xu, and W. Lu, Investigation of Microstructure and Mechanical Properties of Hot Worked NiAl Bronze Alloy with Different Deformation Degree, *Mater. Sci. Eng. A*, 2015, **643**, p 17–24
33. F.J. Humphreys and M.G. Ardakani, Grain Boundary Migration and Zener Pinning in Particle-Containing Copper Crystals, *Acta Mater.*, 1996, **44**(7), p 2717–2727
34. E.A. Culpan and G. Rose, Microstructural Characterization of Cast Nickel Aluminium Bronze, *J. Mater. Sci.*, 1978, **13**, p 1647–1657
35. E. Çadirli and M. Gündüz, The Dependence of Lamellar Spacing on Growth Rate and Temperature Gradient in the Lead-Tin Eutectic Alloy, *J. Mater. Process. Technol.*, 2000, **97**, p 74–81
36. Q. Zhang, J. Chen, X. Lin, H. Tan, and W.D. Huang, Grain Morphology Control and Texture Characterization of Laser Solid Formed Ti6Al2Sn2Zr3Mo1.5Cr2Nb Titanium Alloy, *J. Mater. Process. Technol.*, 2016, **238**, p 202–211
37. H.-H. Fu, D.J. Benson, and M.A. Meyers, Analytical and Computational Description of Effect of Grain Size on Yield Stress of Metals, *Acta Mater.*, 2001, **49**(13), p 2567–2582
38. B.E. Carroll, T.A. Palmer, and A.M. Beesea, Anisotropic Tensile Behavior of Ti–6Al–4 V Components Fabricated with Directed Energy Deposition Additive Manufacturing, *Acta Mater.*, 2015, **87**, p 309–320
39. C. Shen, Z. Pan, D. Cuiuri, B. Dong, and H. Li, In-Depth Study of the Mechanical Properties for Fe3al based Iron Aluminide Fabricated using the Wire-Arc Additive Manufacturing Process, *Mater. Sci. Eng. A*, 2016, **669**, p 118–126
40. A.A. Antonysamy, J. Meyer, and P.B. Prangnell, Effect of Build Geometry on the β-Grain Structure and Texture in Additive Manufac-

ture of Ti-6Al-4V by Selective Electron Beam Melting, *Mater. Charact.*, 2013, **84**, p 153–168

41. T. Murray, S. Thomas, Y. Wu, W. Neil, and C. Hutchinson, Selective Laser Melting of Nickel Aluminium Bronze, *Addit. Manuf.*, 2020, **33**, p 101122

42. T. Wolf, Z. Fu, and C. Körne, Selective Electron Beam Melting of an Aluminum Bronze: Microstructure and Mechanical Properties, *Mater. Lett.*, 2019, **238**, p 241–244